A viscoelastic adhesive epicardial patch for treating myocardial infarction

Xiao Lin[1,9], Yue Liu[2,9], Aobing Bai[3,9], Huanhuan Cai[3,9], Yanjie Bai[4], Wei Jiang[3], Huilin Yang[1,5], Xinhong Wang[3], Lei Yang[1,5,8]*, Ning Sun[3,6,7]* and Huajian Gao[2]*

Acellular epicardial patches that treat myocardial infarction by increasing the mechanical integrity of damaged left ventricular tissues exhibit widely scattered therapeutic efficacy. Here, we introduce a viscoelastic adhesive patch, made of an ionically crosslinked transparent hydrogel, that accommodates the cyclic deformation of the myocardium and outperforms most existing acellular epicardial patches in reversing left ventricular remodelling and restoring heart function after both acute and subacute myocardial infarction in rats. The superior performance of the patch results from its relatively low dynamic modulus, designed at the so-called 'gel point' via finite-element simulations of left ventricular remodelling so as to balance the fluid and solid properties of the material.

schaemic heart disease remains the most fatal cause of death worldwide. Cardiac patches, made from biomaterials or biological substances, and sometimes in combination with cells or drugs, offer a potential treatment for severe myocardial infarction (MI) and subsequent heart failure[1–6]. The biomaterial-based acellular epicardial patch is designed to passively restrain the infarct area of the myocardium following MI, which functions to reduce myocardium wall stress and subsequently prevent left ventricular dilation and remodelling. Although the therapeutic effects of various acellular epicardial patches on MI have been reported[5,7–17] and the benefits of mechanical support from such patches to the myocardial wall have been established[1,7,13–17], the optimum patch design is still unknown due to the lack of understanding of the mechanisms involved in limiting left ventricular remodelling and restoring cardiac function following MI[17,18]. In fact, it is not even clear whether the appropriate patch stiffness exists. The patches reported in the literature to be effective in reducing left ventricular dilation or preserving cardiac function to different extents have stiffness values varying from tens of kilopascals to tens of megapascals[5,8,9,11,12,19–21]. This ambiguity calls for a more rational design of the acellular epicardial patch that could maximize the mechanical benefit and subsequent therapeutic efficacy for the infarcted myocardium. Here, we introduce a simulation-guided strategy to design and develop a type of self-adaptive epicardial patch that accommodates the time-varying deformation of the beating heart and maintains reliable efficacy in restraining ventricular dilatation and preventing adverse left ventricular remodelling and cardiac failure after MI.

Finite-element modelling of the patch under pre-stretch

Ideally, the patch should balance between restraining the normal cardiac loop and providing protection against the adverse dilatation cascade. When seeking materials for mechanical support in biological systems, previous studies focused on the compatibility of static elastic properties, such as stiffness[22], which is insufficient in the cardiovascular system. Due to the time-varying geometry of the system, applying the patch at different moments can set different reference points for deformation, thus introducing different amounts of pre-deformation into the patch, with a non-trivial mechanical effect. Along this line, we constructed a finite-element ventricle infarction model with a patch with pre-deformation, characterized by a pre-stretch factor λ^{pre} (a sketch of the model is shown in Fig. 1a, and the detailed setup is described in the Methods), with which simulations of both cardiac loop and dilatation remodelling were performed.

First, we studied how the elastic patch with different stiffness and pre-stretch characteristics could influence the cardiac cycle. Supplementary Fig. 1a shows some typical simulated pressure–volume loops. The general influence of patch elasticity on stroke volume is summarized in Fig. 1b. Apart from the fact that higher patch stiffness decreases the stroke volume, a major observation was the strong effect of the pre-stretch, especially at the high stiffness regime where pre-stretch can severely deform the ventricle and restrain the filling. This can be a major drawback for high stiffness as pre-stretch is usually very difficult to avoid.

We also conducted a ventricular remodelling simulation to investigate the left ventricular dilatation with the elastic patch, where the change in the end-diastole ventricular cavity volume was computed (Fig. 1c). Some distributions of the lengthening factor λ^g (see Methods for a definition) are shown in Fig. 1d, and their developments with time are shown in Supplementary Fig. 2. As can be intuitively expected, higher patch stiffness and pre-stretch brought better confinement against the lengthening and dilatation. However, it should be noted that, for the case without pre-stretch ($\lambda^{pre} = 1$), at a high stiffness regime the confinement reached a plateau, indicating saturation of the stiffness. In comparison, in the presence of pre-stretch, the confinement was substantially enhanced.
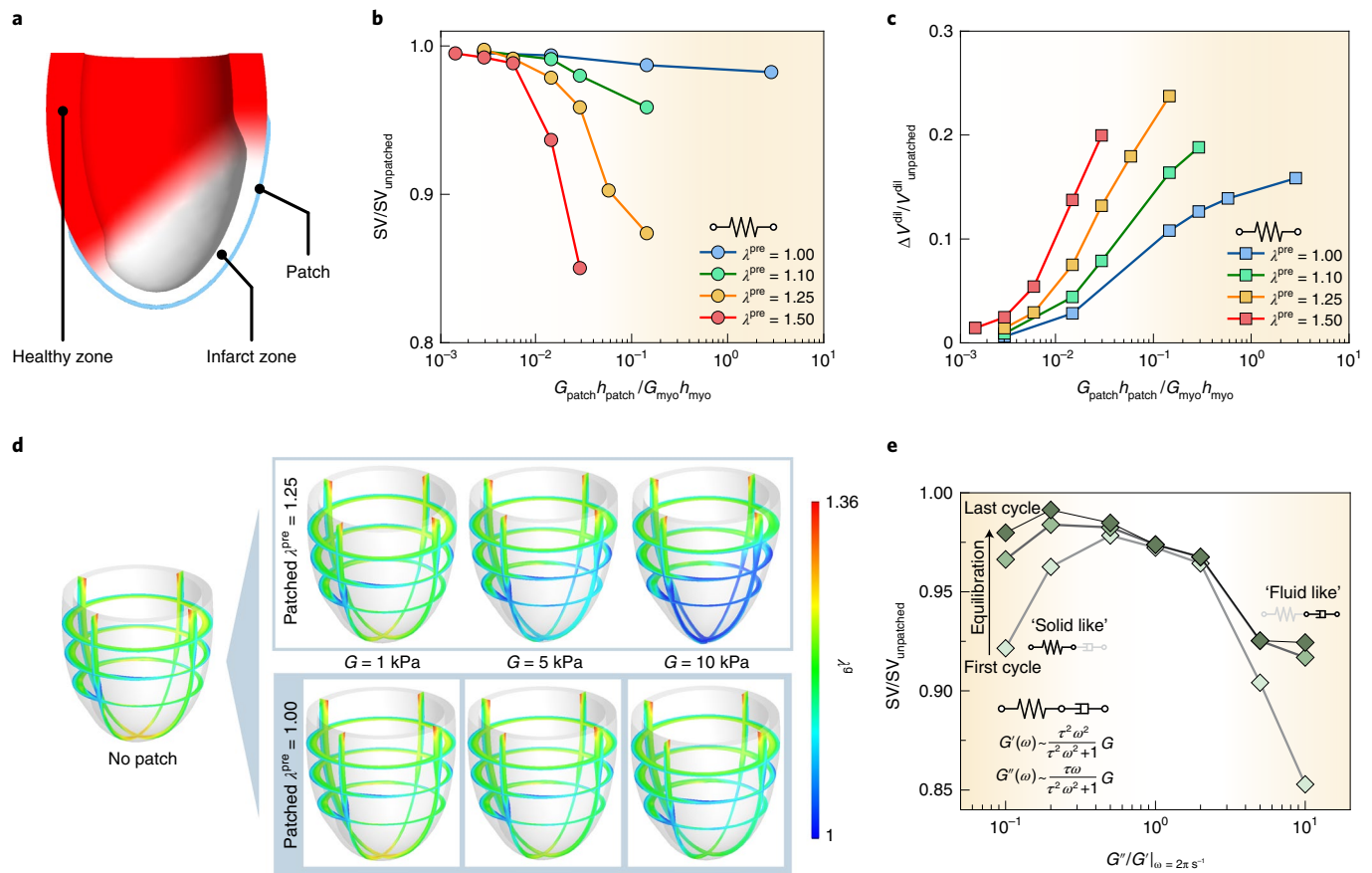
Fig. 1 | Finite-element simulation model for the epicardial patch. a, Illustration of the model geometry. The infarct zone is located around the apex and part of the ventricle wall, with a thickness that is half that of the healthy zone. **b**, Relationship between stroke volume (SV) (15 mmHg EDP) and patch shear modulus at different pre-stretch levels, with SV normalized by the unpatched value, and modulus normalized by the end-diastole myocardium shear modulus (44 kPa in our model) and patch-to-myocardium thickness ratio (h_{patch}/h_{myo} = ~1/8). **c**, Relationship between the dilated cavity volume V^{dil} and patch shear modulus at different pre-stretch levels; $\Delta V^{dil} = V^{dil} - V^{dil}_{unpatched}$ denotes the difference in the dilated cavity volume with and without the patch. **d**, Distribution of the lengthening factor after dilatation under various values of patch stiffness and pre-stretch, where $\lambda^{g} = 1$ corresponds to no local lengthening. The patch is not shown for clarity. **e**, Effect of viscous dissipation with a Maxwell viscoelastic patch with $\lambda^{pre} = 1.5$ initially. The x axis shows the ratio between the loss and storage modulus at the working frequency of $f = 1\,s^{-1}$ with $G'(2\pi f) = 10\,kPa$. The y axis is the SV ratio to the unpatched case. The three curves show SV from three different cycles during the equilibration. The bottom curve is the computed first cycle, the middle curve is an intermediate cycle and the top curve is the converged cycle.

Design with fluid-like material near the gel point

Combining the cyclic loading and left ventricular remodelling simulations, we noticed that a stiff elastic patch appears to not be ideal due to the risk of over-reducing the stroke volume whenever a pre-stretch exists (for example, when the patch is applied near end-systole or when the ventricle grows or remodels). In comparison, a patch with $G_{patch}h_{patch}/G_{myo}h_{myo}$ (where G denotes the shear modulus and h the thickness, the subscript 'patch' denotes the patch, and 'myo' the myocardium) in the range of 10^{-2}–10^{-1}, together with about 10–20% pre-stretch could both resist dilatation and stay robust on stroke volumes around pre-stretch perturbations (Fig. 1b,c). However, tuning the pre-stretch becomes another challenge. Since the ordinary magnitude of myocardial strain during a heartbeat is also approximately ±10–20% (Supplementary Fig. 1b), one solution is to replace the solid elastic patch with a fluid-like material, with the storage modulus being minimal at zero frequency (static modulus) yet finite at working frequency. In this way, the patch generates stress only according to the dynamic variation of strain, instead of the absolute deformation, and effectively, we could obtain a pre-stretch near the desired value. Because viscoelasticity is usually accompanied

by viscous dissipation, we used the Maxwell fluid model on the patch with $\lambda^{pre} = 1.5$ and computed the associated stroke volume, as presented in Fig. 1e. It was found that, at working frequency, the stroke volume dropped promptly as the order of magnitude of G''/G' approached 10^{1}, whereas, near 10^{-1}, the ventricle had a longer exposure to the lowered stroke volume under initial pre-stretch during the equilibration process, from which we concluded that the patch would be most adaptive to cardiac functioning as G''/G' stayed close to 1. Although here we only considered the working frequency $f = 1\,s^{-1}$, to accommodate the varied biological heartbeat frequencies under different physiological conditions, it is desirable to have $G''/G' \sim 1$ for a wider frequency range, which can be satisfied at the so-called gel point[23,24]. That is, a material near the gel point can not only provide necessary fluidity, but can also avoid excessive dissipation. With this design (that is, $G_{patch}h_{patch}/G_{myo}h_{myo} \sim 10^{-2}$–$10^{-1}$ and $G''/G' \sim 1$), the patch is expected to balance between restraining the dilatation and maintaining the normal cardiac function. Moreover, since both $G_{patch}h_{patch}/G_{myo}h_{myo}$ and G''/G' are non-dimensional parameters, the above conclusions regarding their effects should remain independent of the size or temporal scale of the ventricle system.
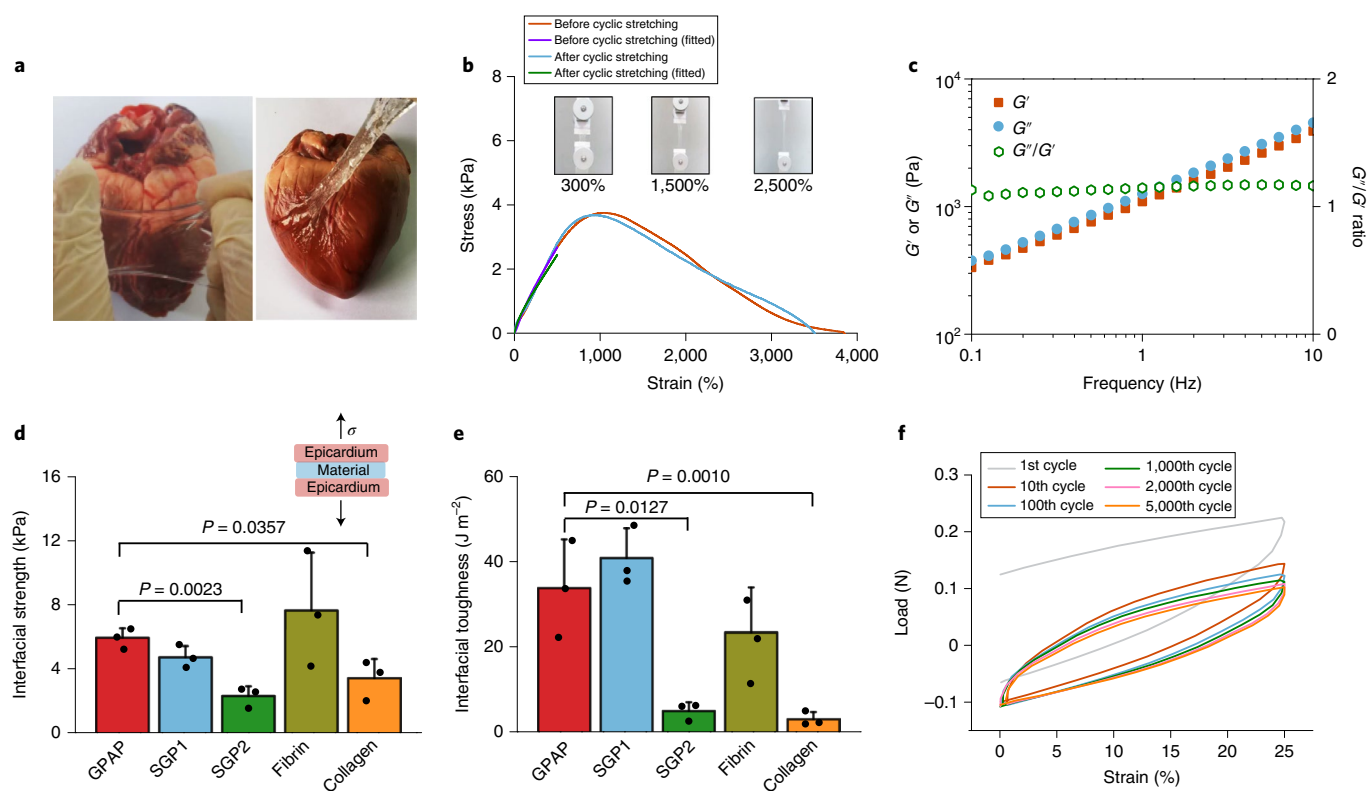
Fig. 2 | GPAP for MI treatment. a, A stretched GPAP film (left) adhering firmly on a pig epicardium (right). **b**, Stress–strain curves of the GPAP under a strain rate of $\dot{\varepsilon} = 0.143\ s^{-1}$ before and after cyclic stretching and either fitted or not fitted with the neo-Hookean model to 500% strain. Inset, photos of the GPAP stretched at different ratios. **c**, Dependence of G', G'' and the G''/G' ratio of the GPAP on the frequency of oscillation. **d**, Material/epicardium interfacial strengths. Inset, schematic of the adhesion test. **e**, Material/epicardium interfacial toughnesses. **f**, Load–strain curves of the GPAP (pre-strain of 50%) at different stretching cycles up to 5,000 cycles. In **d** and **e**, means ± s.d. of the original data are presented ($n = 3$ distinct samples for all groups). A two-tailed unpaired Student's t-test was used for comparison between groups.

Simulation-guided gel-point adhesive patch

To validate the above simulation-guided design, we developed a gel-point adhesive patch (GPAP) possessing viscoelastic traits, as suggested by the theoretical predictions (Fig. 2a,b, Supplementary Fig. 3 and Supplementary Video 1). In essence, the GPAP is an ionically crosslinked transparent starch hydrogel (Supplementary Fig. 4), whose dynamic moduli (Fig. 2c) and stress–relaxation behaviours (Supplementary Fig. 5) fit well with the power law relations given by the crosslinking polymer gel equation at the gel point[23,24]. The GPAP has a markedly higher stretchability (~3,500% measured at a strain rate of $0.143\ s^{-1}$) compared with most conventional or engineered hydrogels[25], and its stretching behaviour under a constant strain rate also fits well with the neo-Hookean model (Fig. 2b). We verified that the GPAP exhibits almost identical loss and storage moduli ($G''/G' \sim 0.95$–1.15; Fig. 2c) over a wide range of values for storage time (up to 60 days), temperature (20–60 °C), humidity (40–80% relative humidity), shear strain (1–100%) and frequency (0.1–10 Hz) (Supplementary Figs. 6 and 7a,b). This stable gel-point behaviour is likely to associate with the reversible water retention capability of the GPAP (Supplementary Fig. 7c–e). The GPAP is also injectable (Supplementary Video 3), and its moduli can be adjusted by slightly tuning the starch concentration, enabling more versatility for future clinical uses such as minimally invasive surgery and personalized treatment. According to the theoretical design, the GPAP was prepared to possess storage moduli of ~3 kPa and ~1 kPa at the oscillation frequencies close to the rat (~6 Hz) and human (~1.25 Hz) heart rates, respectively, within the body temperature range of 37–40 °C (Fig. 2c and Supplementary Fig. 8).

Also, as shown by both theoretical and experimental assessments (Supplementary Figs. 9 and 10), the GPAP has balanced self-adhesiveness and stiffness, guaranteeing robust but compliant adhesion on the beating heart, and thus enabling a suturing-free attachment to the cyclically deforming epicardium with high conformability (Supplementary Video 2 and Supplementary Fig. 10a). The adhesiveness of the GPAP is higher than that of commercially available collagen and similar to that of fibrin glue, as shown by the strength and interfacial toughness results of adhesion tests (Fig. 2d,e). This strong adhesiveness of the GPAP is probably attributed to the substantial amount of energy dissipated from the progressive unzipping of ionically crosslinked starch molecules during peeling (Supplementary Fig. 10b)[25,26]. In contrast, although the commercial cyanoacrylate glue has much higher adhesiveness than the GPAP and other tissue glues (Supplementary Fig. 11), its high stiffness is not compliant enough to accommodate the cyclic deformation of the beating heart, causing a 100% rate of death in rats after 2 d of implantation (Supplementary Fig. 12).

The GPAP is self-adaptive and safe for MI treatment

We further conducted a cyclic tensile test on the GPAP at a frequency of 1.25 Hz and strain of 25% to mimic the dynamic deformation of the human heartbeat. The GPAP is mechanically stable under cyclic loading, as its neo-Hookean tensile behaviour remains identical after 2,000 cycles (Fig. 2b). More importantly, the stress converges to a steady state within 5,000 cycles following a rapid decay of stress within the first 100 cycles (Fig. 2f), and the steady state stress appears to be independent of the pre-stretch (Supplementary Fig. 13). This mechanical behaviour is in agreement with the aforementioned
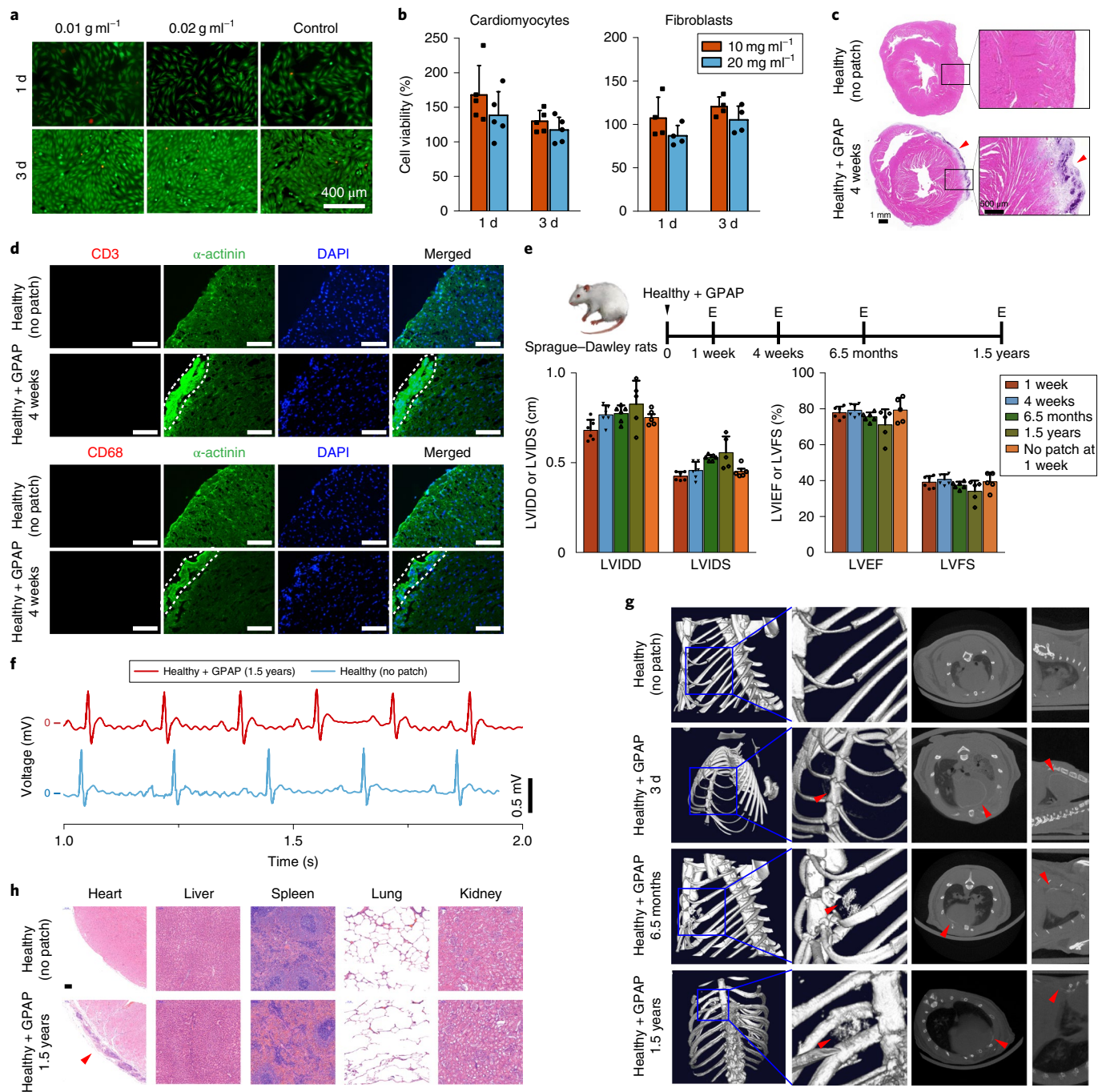
Fig. 3 | Biocompatibility and stability of the GPAP. a, Fluorescence micrographs of H9C2 rat cardiomyocytes after being cultured with the GPAP extracts or regular cell culture media for 1 and 3 d. **b**, Viability of H9C2 rat cardiomyocytes (left) and NIH/3T3 fibroblasts (right) when cultured with the GPAP extracts for 1 and 3 d versus a control group (viability set as 100%). Means ± s.d. of the original data are presented ($n = 5$ for the cardiomyocyte groups; $n = 4$ for the fibroblast groups). A two-tailed unpaired Student's t-test was used for comparison between the concentration groups after the same culturing time, and no significant difference ($P > 0.05$) was found. **c,d**, Haematoxylin and eosin (**c**) and CD3 and CD68 immunofluorescence staining (**d**) of healthy heart tissue after patching with the GPAP for 4 weeks. The position of the GPAP is outlined by a white dotted line in **d**. The experiments were repeated three times independently, and each image is representative of at least six images taken. Scale bars (**d**), 100 μm. **e,f**, Echocardiographic assessment (**e**) and electrocardiograms (**f**) of healthy rats with and without the GPAP for 1.5 years. In **e**, an 'E' on the timeline marks each time point at which echocardiographic assessment was performed. Means ± s.d. of the original data are presented ($n = 6$ for the healthy + GPAP group; $n = 5$ for the healthy groups). **g**, Micro-computed tomography (CT) images of the healthy heart patched with the GPAP for up to 1.5 years. **h**, Haematoxylin and eosin staining of the important organs of the healthy rats with and without the GPAP for 1.5 years. Scale bar, 100 μm. In **c**, **g** and **h**, the position of the GPAP is indicated by red arrowheads.

simulation-based design, and such a unique self-stabilization ability, attributed to the gel-point characteristic of the material, indicates that the GPAP has a self-adaptive stiffness that yields appropriate stress to the myocardium in response to the cyclic deformation magnitude. The self-adaptive capability is key to circumventing the reliability issue associated with the magnitude of pre-stretch during
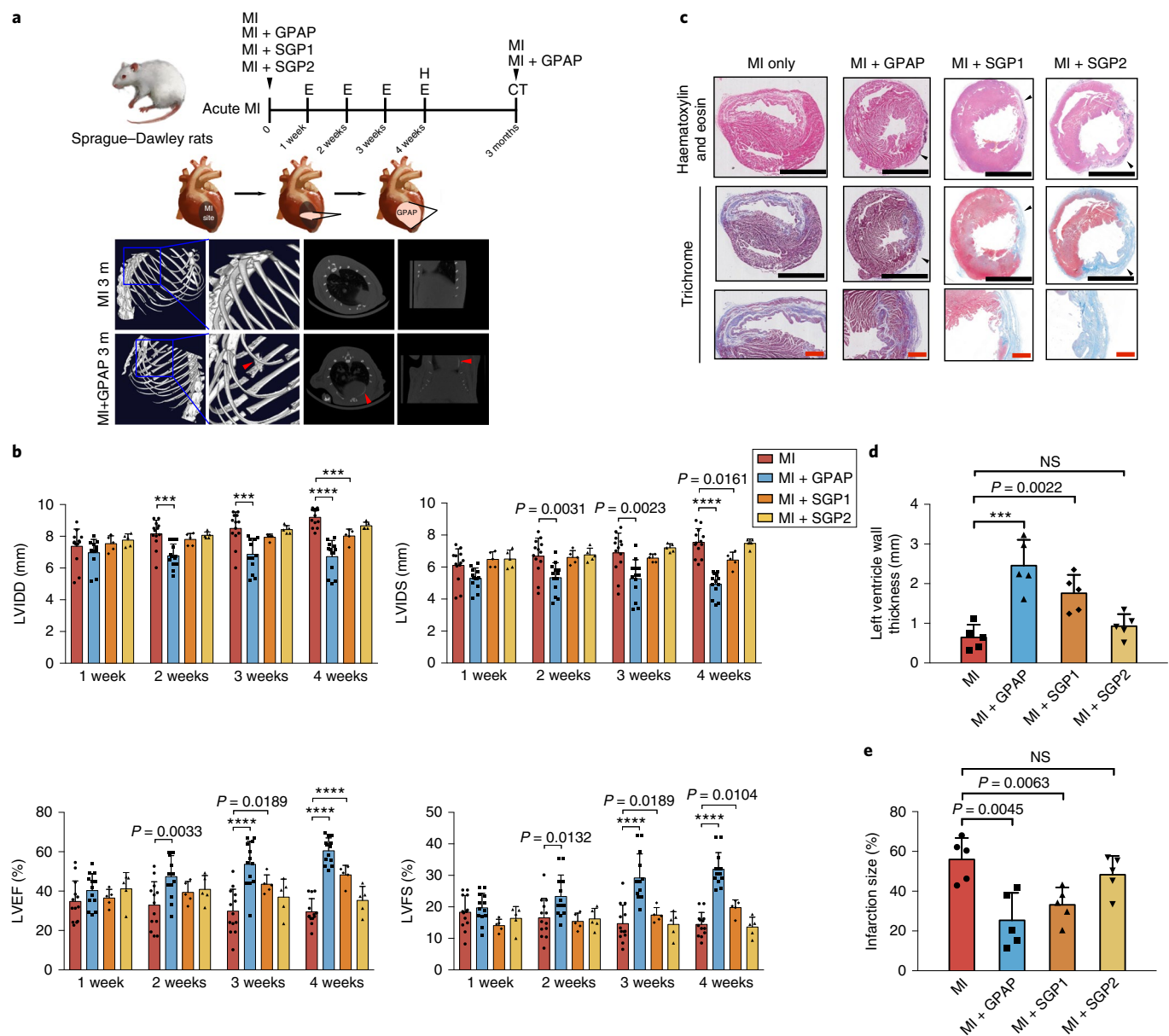
Fig. 4 | The GPAP improved heart function and reduced pathological cardiac remodelling after acute MI. a, Top, experimental design. The treatment effects of the GPAP, SGP1 and SGP2 were tested in an acute model, by echocardiography (E) and histology (H), between weeks 1 and 4. In addition, micro-CT was performed to compare MI rat hearts with and without GPAP after 3 months. Bottom, CT images (with GPAP indicated by red arrowheads). **b**, Echocardiographic assessment of cardiac function 4 weeks after patching with the GPAP (n = 13), SGP1 (n = 5) or SGP2 (n = 5), or without treatment (n = 13) in acute MI models. **c**, Haematoxylin and eosin and Masson's trichrome staining of heart sections 4 weeks after patching with the GPAP, SGP1 or SGP2 in acute models. Black arrowheads indicate gel patches. Scale bars, black, 5 mm; red, 1 mm. **d,e**, Left ventricle wall thickness (**d**) and infarction size (**e**) 4 weeks after gel patch operation in acute MI models (n = 5). In **b**, **d** and e, means ± s.d. of the original data are presented (NS, non-significant (P > 0.05); ***P < 0.001; ****P < 0.0001, two-tailed unpaired Student's t-test).

patch deployment, which is difficult to optimize and remains a challenge for existing ventricular restraint devices[17,27,28], leading to a class of patches that are mechanically safe to be applied on the myocardium regardless of the magnitude of the pre-stretch and diastole or systole phases.

The GPAP is also biologically safe in vivo due to its high biocompatibility at cell, tissue and organ levels. Cytocompatibility evaluated by culturing cardiomyocytes and fibroblasts with GPAP extracts revealed no toxic effect on cell viability (Fig. 3a) and proliferation (Fig. 3b). After patching on healthy rat hearts, the GPAP was safe (Supplementary Fig. 12) and did not induce any apparent heart tissue damage (Fig. 3c and Supplementary Fig. 14) nor immunological

reactions, such as the accumulation of T cells and macrophages, within the heart tissue and at the epicardium–patch interface during the 28 d of the observation period (Fig. 3d). Echocardiography examinations on healthy rats with or without the GPAP showed that the key cardiac function indicators, including left ventricular internal diastolic diameter (LVIDD), left ventricular internal systolic diameter (LVISD), left ventricular ejection fraction (LVEF) and left ventricular fractional shortening (LVFS) remained stable within the 1.5-year observation period (Fig. 3e). The electrocardiogram results of healthy rats patched with the GPAP for 1.5 years were comparable to those of healthy rats without patching (Fig. 3f and Supplementary Figs. 25 and 26). Long-term micro-computed
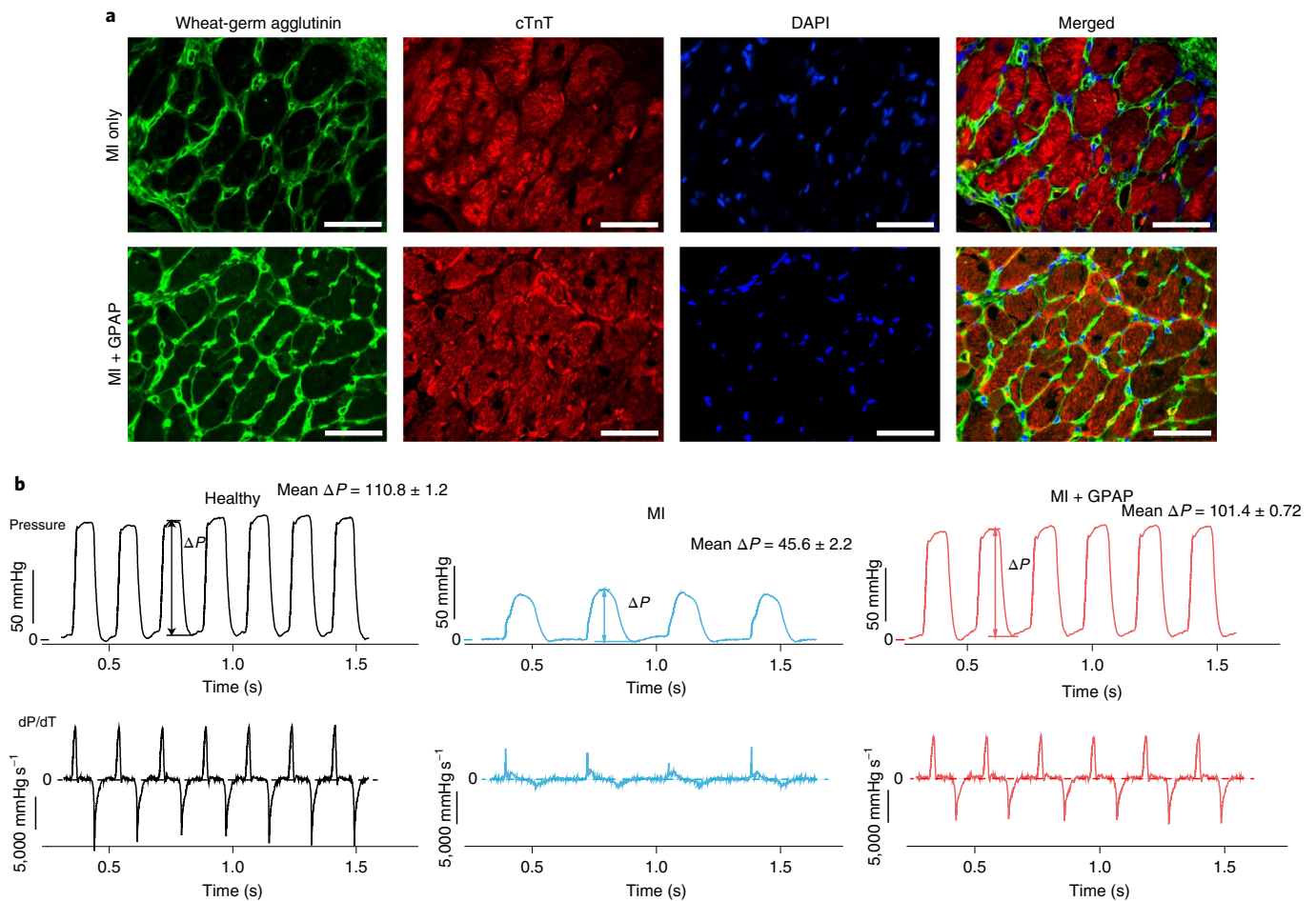
Fig. 5 | The GPAP reduced myocyte hypertrophy and improved left ventricular systolic and diastolic functions after acute MI. a, Heart sections were stained with wheat germ agglutinin (green), cardiac troponin T (cTnT, red) and DAPI (blue) 4 weeks after operation in acute MI models. Scale bars, 50 μm. The experiments were repeated 3 times independently, and each image represents at least 12 images taken. **b**, Haemodynamic measurement of left ventricular function (pressure and its changing rate) 4 weeks after patching with the GPAP (right) or no patching (middle) in acute MI models. Healthy rats served as a control (left). Here, the ΔP values are defined as the difference between the peak pressure of each stroke and the lowest pressure after relaxation. Means ± s.d. were calculated on the strokes shown.

tomography tracking revealed that the GPAP could adhere to the myocardium and did not completely degrade within the 1.5-year observation period (Fig. 3g). Although thinning of the GPAP adhered on the myocardium was observed after 1.5 years, probably due to the enzymatic degradation of starch by the amylase existing in pleural fluids[29], degradation was very slow and appeared to be minimal in the first few weeks, since the thickness of the GPAP was not significantly decreased (Supplementary Fig. 14). Furthermore, histological examination indicated that neither the GPAP nor its degradation products caused any apparent pathological changes within the important organs (heart, liver, spleen, lung and kidneys) after patching for 1.5 years (Fig. 3h).

The GPAP reverses left ventricular remodelling after MI

Next, we patched the GPAP on the hearts of acute or subacute MI rat models established by left anterior descending (LAD) coronary artery ligation (Supplementary Fig. 15). Cardiac function and structure were assessed by echocardiography and histology at different time points after MI (Fig. 4a). In our experiment, the selection of $G_{patch}h_{patch}/G_{myo}h_{myo} = 8.8 \times 10^{-2}$ (the rat myocardium stiffness was estimated from ref. [30] and the thickness was measured from Supplementary Fig. 14) is in the expected optimal range from our simulation, and this parameter ($G_{patch}h_{patch}$) was shown to remain

unchanged for at least eight weeks (Supplementary Fig. 16). To validate the therapeutic effect of the simulation-optimized GPAP and elucidate the underlying mechanisms, two biocompatible starch gel patches (SGPs) with almost identical composition (for preparations, see Methods, and for their cytocompatibility, see Supplementary Fig. 17), but different mechanical properties (Supplementary Fig. 18) were also tested. SGP1 had similar gel-point characteristics to the GPAP, while SGP2 was more solid-like (that is, $G' > G''$). Since both SGPs were much stiffer than the GPAP (storage moduli: SGP2 >> SGP1 > GPAP), the parameter $G_{patch}h_{patch}/G_{myo}h_{myo}$ for SGP1 (~0.58) and SGP2 (~4.23) did not fall within the simulation-suggested optimal range.

Among the 4-week echocardiographic results of all groups, the MI + GPAP group showed the smallest values for LVIDD and LVISD (Fig. 4b and Supplementary Fig. 19a), indicating less dilation of the heart, and cardiac remodelling after mechanical treatment. LVEF and LVFS values were among the highest compared with those of the MI only and two SGP groups at week 4 (Fig. 4b), indicating better improvement of left ventricular heart function after patching with the GPAP on the infarcted heart in acute MI.

Histological examinations by haematoxylin and eosin and trichrome staining four weeks after MI showed that the left ventricle wall was thicker in the GPAP group and preserved substantially more
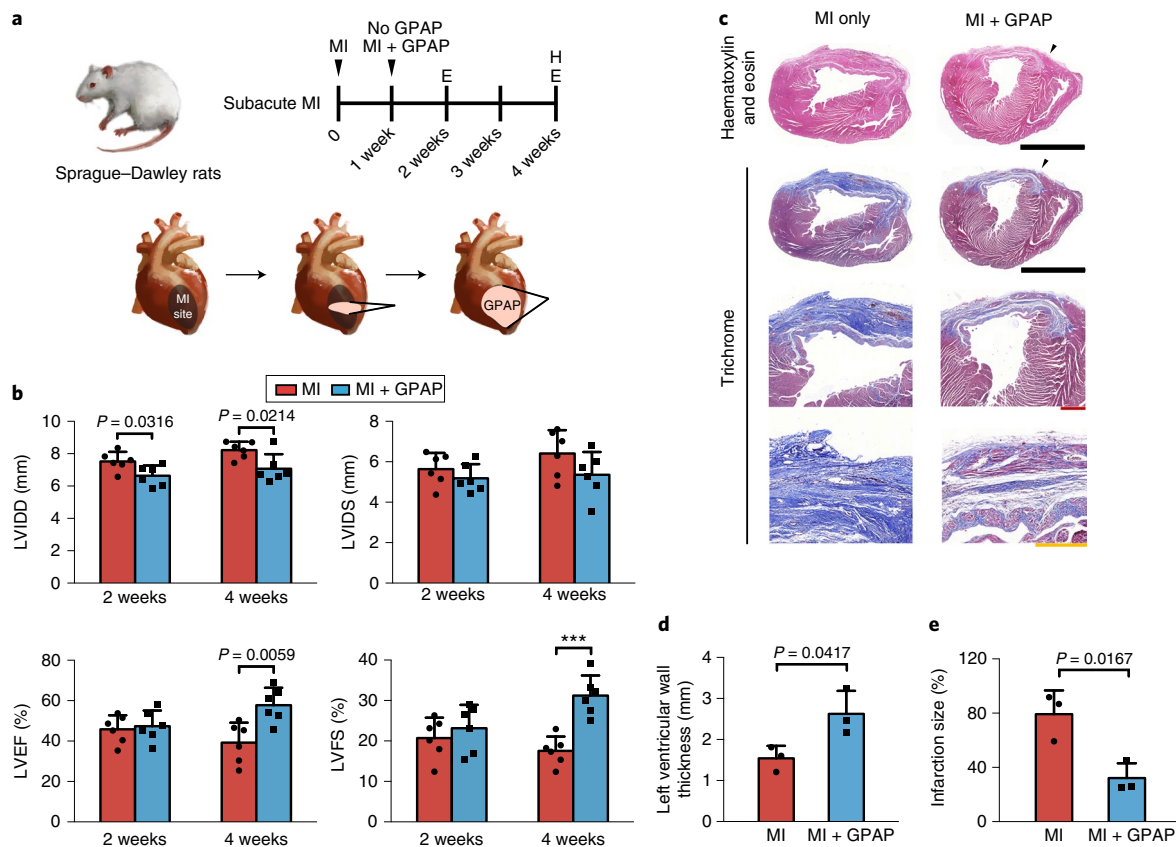
Fig. 6 | The GPAP improved heart function and reduced pathological cardiac remodelling after subacute MI. a, Experimental design for testing the treatment effects of the GPAP in subacute MI models. **b**, Echocardiographic assessment of cardiac function 2 and 4 weeks after MI with and without the GPAP ($n=6$ for each) in subacute MI models. **c**, Haematoxylin and eosin and Masson's trichrome staining of heart sections 3 weeks after patching with the GPAP (4 weeks after MI) versus no patching in subacute MI models. Black arrowheads indicate gel patches. Scale bars, black, 5 mm; red, 1 mm; yellow, 500 μm. **d,e**, Left ventricle wall thickness (**d**) and infarction size (**e**) 3 weeks after patching with the GPAP (4 weeks after MI) versus no patching in subacute MI models ($n=3$). In **b**, **d** and **e**, means ± s.d. of the original data are presented (***$P<0.001$; two-tailed unpaired Student's t-test).

myocardia than those in the MI and two SGP groups (Fig. 4c,d). Fibrosis was also significantly alleviated in the MI+GPAP group (Fig. 4c), suggesting that the events of cardiomyocyte death and subsequent replacement with fibrotic tissues in the damaged area were greatly reduced after immediate application of the GPAP after MI. Moreover, morphological evaluation showed that the left ventricle wall thickness increased (Fig. 4d) and the infarction size decreased (Fig. 4e) significantly in the MI+GPAP group compared with the MI and two SGP groups. These results show that the unique mechanical properties of the GPAP alone, without support from any additional biological agents or cells, had a substantial reversing effect on pathological cardiac remodelling after acute MI. Micro-computed tomography evaluation showed that the GPAP was stably patched on the epicardium at three months after MI (Fig. 4a). Furthermore, the GPAP application reduced myocyte hypertrophy at the border zone four weeks after MI (Fig. 5a). Haemodynamic measurements of MI hearts with and without the patched GPAP at four weeks showed that the GPAP significantly enhanced left ventricular pressure and the maximum value of rate of pressure change (dP/dt, Fig. 5b) while also decreasing the left ventricular relaxation time constant (Supplementary Fig. 20), indicating markedly improved left ventricular systolic and diastolic function when the GPAP was applied after MI. Simulation results of local changes in left ventricle wall stress also revealed that there was a non-trivial drop in the passive stress at end diastole near the border zone of MI when the patch was applied (Supplementary Fig. 1c). Immunostaining of CD3 and CD68 cells on heart tissues at

four weeks post-MI showed that the GPAP did not induce an apparent immunoresponse (Supplementary Fig. 21). To our knowledge, in terms of therapeutic efficacy defined by the overall changes in LVEF, LVFS and infarction size before and after epicardial patch treatment for MI in the rat model, the present GPAP surpasses many other biomaterial-based acellular patches developed so far[8,10,12,31–34], as well as extracellular matrix-based acellular patches[35,36] (Supplementary Fig. 22 and Supplementary Tables 1 and 2), and even some cell-loaded and/or therapeutic agent-loaded patches (Supplementary Table 3).

We also examined the therapeutic efficacy of the GPAP on subacute MI, which is clinically common for patients without prompt treatment after MI. Here, the GPAP was patched on the MI site one week after LAD coronary artery ligation, and echocardiographic and histological evaluations were performed (Fig. 6a). Although the values of LVIDD and LVISD did not change significantly, LVEF and LVFS showed clear improvement in the MI+GPAP group compared with the MI group (Fig. 6b and Supplementary Fig. 19b). We also found that the left ventricle wall was thicker in the MI+GPAP group than in the MI group (Fig. 6c,d) four weeks after subacute MI (that is, three weeks after patching). Morphological evaluation showed that in the MI+GPAP group, the infarction size decreased significantly compared with the MI group (Fig. 6e). Again, in terms of the overall changes in LVEF, LVFS and infarction size, the therapeutic efficacy of the GPAP for subacute MI was better than many other biomaterial-based acellular patches[19,37–40] and most extracellular matrix-based acellular patches[35,41–43] developed so far
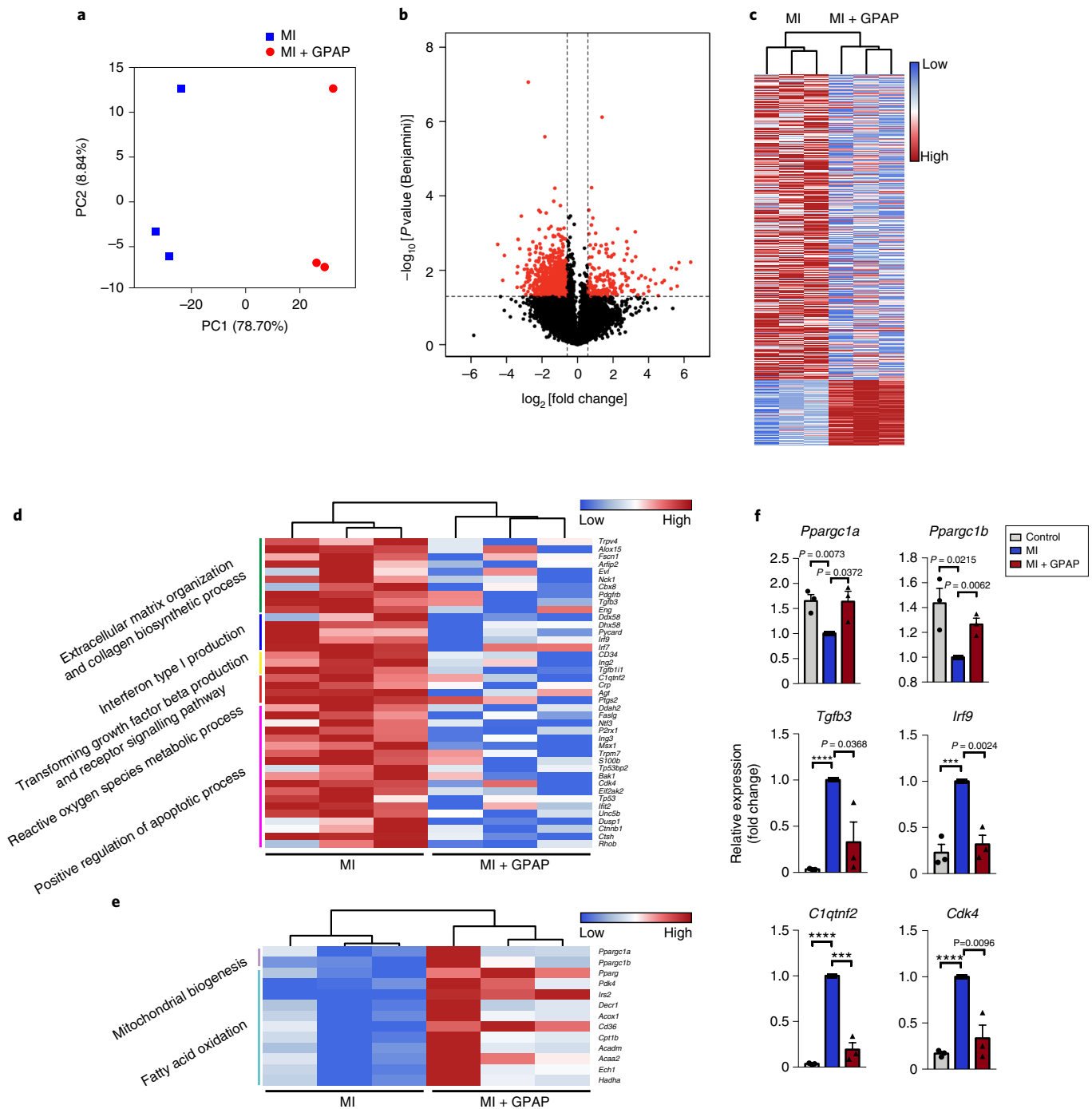
Fig. 7 | The GPAP reduced pathological cardiac remodelling after acute MI from transcriptome levels. a, Principal component (PC) analysis of transcriptomes of the infarct area from the acute MI and acute MI + GPAP groups ($n = 3$ per group). **b**, Volcano plot of all of the expressed genes from acute MI patched with the GPAP versus without ($n = 3$ per group). The vertical dashed lines represent the border of the gene expressions greater than 1.5 times fold-change versus the control. Dots above the horizontal dashed line have P values less than 0.05. **c**, Differentially expressed genes between the MI and MI + GPAP groups (red, upregulated; blue, downregulated; cut-off > 1.5; $P < 0.05$; $n = 3$ per group). The web-based platform OmicsBean—a microarray data analysis system—was used for raw data variance modelling and statistical testing, as well as for gene ontology analyses and principle component analysis. **d,e**, Expression of the ventricular remodelling-related genes between the MI and MI + GPAP groups (red, upregulated; blue: downregulated, cut-off > 1.5; $P < 0.05$; $n = 3$ per group). After applying GPAP, selected downregulated genes shown in **d**, while selected upregulated genes shown in **e**. **f**, Expression of *Ppargc1a*, *Ppargc1b*, *Tgfb3*, *Irf9*, *C1qtnf2* and *Cdk4* in the control, MI and MI + GPAP groups 4 weeks after MI ($n = 3$ per group). Means ± s.d. of the original data are presented (***$P < 0.001$; ****$P < 0.0001$, two-tailed unpaired Student's t-test).

(Supplementary Fig. 22 and Supplementary Tables 1 and 2). Also, the GPAP alone has similar or better therapeutic efficacy compared with some of the therapies using cells and/or therapeutic agents, even when a fibrotic scar was formed after subacute MI (Supplementary Table 3).

The GPAP reduces pathological cardiac remodelling after acute MI

From the collective data of both acute and subacute MI experiments, the GPAP shows a marked therapeutic efficacy for ischaemic

heart diseases. To further confirm this therapeutic efficacy at the molecular level, we performed whole-transcriptome analysis by RNA sequencing (RNA-Seq) using heart tissues of the infarct site in the MI and MI + GPAP groups four weeks after acute MI. Heart tissues from the same location on the left ventricle from healthy rats were used as controls. Differences in the messenger RNA (mRNA) levels in the transcriptome between the infarct regions of the MI and MI + GPAP groups were thoroughly examined using both principal component analysis and a volcano plot, which showed a separation of the transcriptomes (Fig. 7a–c). Compared with the MI group, the analysis revealed 890 downregulated genes at the MI + GPAP infarction site. These genes were involved in extracellular matrix and collagen biosynthesis, interferon production, the reactive oxygen species metabolic process and the apoptotic process (Fig. 7d). There were 190 upregulated genes in the infarct region of the MI + GPAP group, some of which were involved in mitochondrial biogenesis and fatty acid oxidation, such as *Ppargc1a* and *Ppargc1b* (Fig. 7e). We further validated the mRNA expression level from the RNA-Seq results by quantitative PCR (Fig. 7f). These results indicated that, at the transcriptome level, the unique gel-point properties of the GPAP induced expression changes in molecular pathways leading to decreased fibrosis, apoptosis, inflammation and generation of reactive oxygen species in the infarct zone, and improved the function of mitochondrial metabolism, thereby reducing the overall pathological cardiac remodelling after MI. Immunofluorescence staining of caspase-3 and annexin-V further confirmed a reduced apoptosis level at the border zone of MI after GPAP application, although angiogenesis was not clearly different, as reflected by von Willebrand Factor and α-smooth muscle actin staining (Supplementary Figs. 23 and 24).

This simulation-guided design of epicardial patches points to a critical viscoelastic behaviour at the gel point leading to a self-adaptive dynamic stiffness that balances the fluid and solid properties of the patch in response to cyclic deformation. This understanding reveals a mechanism by which an epicardial patch becomes self-adaptive to the time-varying deformation of heart contraction–relaxation cycles, thereby not only appropriately restraining dilatation but also effectively reversing the decaying cardiac output following MI. Guided by this mechanism, we fabricate a viscoelastic adhesive epicardial patch, which to our knowledge creates a unique and safer solution for treating MI without additional agents or cells. It is also worth mentioning that the fabrication of the GPAP is extremely simple and low in cost (the cost of materials in our laboratory for a 1 cm² GPAP with a thickness of 1 mm is less than a penny). This work paves the way for further investigations, including MI models of large animals and clinical studies, to fully uncover the translational value of the GPAP therapy. The simulation-based approach established here may also lead to the future design of GPAPs that are customized according to a patient's information, including their gender, age, infarction area and individual-specific heart geometry, enabling more precision in treatment with improved simulation algorithms and fabrication techniques of the GPAP for personalized needs. In addition, our findings set a promising mechanism and technology, which can be expanded to further combine biological substances, such as cytokines, cells and even engineered tissues, for perfecting the treatment of ischaemic heart diseases in the future. It should also be noted that, apart from the ventricle system presented above, the mechanical design proposed in this study, which balanced fluidity and solidity, could potentially serve as a general principle to provide mechanical support on cyclic-loaded biological or engineering systems, which usually lack a well-defined reference point for deformation. Finally, although this clinical protocol used a mini-incision for implantation, with the appropriate equipment, an injectable approach can be envisioned with this biomaterial technology.

Methods

Finite-element model setup. We used a truncated ellipsoid as a generic geometrical representation of the human left ventricle, with the semi-axis lengths and height taken from ref. [44]. The semi-axis lengths are 49.25 and 26.85 mm for the epicardial surface, and 42.75 and 19.4 mm for the endocardial surface. The height between the basal plane and the apex point is 63.58 mm. We assumed the material orientations of the myocardium to ramp linearly in the transmural direction, with the fibre angle rotating from $\pi/3$ on the endocardial surface to $-\pi/3$ on the epicardial surface, and the sheet angle from $\pi/4$ to $-\pi/4$ (ref. [45]). On the basal plane, we prescribed zero vertical displacement and, along its edge, we fixed the circumferential displacement[46]. The degree of MI was characterized by an index M that ranges from 0 in the healthy zone to 1 in the infarction zone and varies continuously in a transition zone in between. The stiffness of the myocardium was assumed to change linearly with M[47], and to be twice the normal value in the infarction zone, where the wall thickness and the active contraction were taken as only half of the normal value, corresponding to a mild degree of myocardium remodelling under infarction (Fig. 1a). A tied interface between the ventricle and patch ensured displacement continuity.

We performed two types of simulation. The first was a cyclic loading simulation aimed at characterizing the stroke volume of the ventricle under the effect of infarction and patch. On the endocardial surface, a time-varying pressure $p(t)$ was applied. The simulation included several stages as follows. (1) The initialization stage, where p increased to the end-diastolic pressure (EDP) while the patch deformed plastically. At the end of this stage, the deformation gradient within the patch was recorded as $\mathbf{F}^p$. Then, based on this configuration, a circumferential pre-stretch $\mathbf{F}^{pre} = \lambda^{pre}\mathbf{e}_c \otimes \mathbf{e}_c + (\lambda^{pre})^{-1/2}(\mathbf{I} - \mathbf{e}_c \otimes \mathbf{e}_c)$ was applied to the patch ($\mathbf{e}_c$ is the unit vector in the circumferential direction and $\mathbf{I}$ is the unity tensor). Starting from this point, the total deformation gradient of the patch can be written as $\mathbf{F} = \mathbf{F}^e\mathbf{F}^{pre}\mathbf{F}^p$, where $\mathbf{F}^e$ denotes the subsequent elastic deformation and only $\mathbf{F}^e\mathbf{F}^{pre}$ contributes to the stress generation. (2) The isovolumetric contraction stage, where the active contraction began while the ventricular cavity volume was fixed through a penalty method. (3) The ejection phase after p reached 80 mmHg[48], where a two-element Windkessel model was adopted to simulate the haemodynamics:

$$C\frac{\mathrm{d}p}{\mathrm{d}t} + \frac{p}{R} = -\frac{\mathrm{d}V}{\mathrm{d}t}$$

(V denoting the volume of the cavity while C and R being two constants), which has an analogy with the electrical circuit system. (4) The isovolumetric relaxation stage after the blood flow became reversed ($\mathrm{d}V/\mathrm{d}t \geq 0$), where the cavity volume again was fixed. (5) The filling stage after p reached 4.5 mmHg[48]; the pressure was increased back to the EDP, which was chosen to be 8 mmHg for a healthy ventricle[47] and 15 mmHg in the case of infarction[49]. For all cases, we computed three cycles, which was sufficient for convergence, and then recorded the stroke volume value.

The second type of simulation was a ventricular remodelling test that aimed to study the ventricular dilatation under the infarction conditions and the patch effect. The simulation consisted of two stages: (1) the initialization stage, which was identical to the cyclic loading simulation; and (2) the remodelling stage, during which the myocardial lengthening started to develop under constant endocardial pressure.

For both types of simulations, we modelled the passive elasticity of the myocardium with the Holzapfel–Ogden model[46,50]. In the cyclic loading test, we adopted the time-varying elastance model[51,52] for active contraction. In the left ventricular remodelling test, we adopted a mechanically induced lengthening law[53–57]. In contrast, the patch was first modelled as an incompressible neo-Hookean solid with shear modulus G. To investigate the potential effect of fluidity and viscosity, we also employed the Maxwell fluid model[58]. All simulations were carried out using the open-source package FEBio[59]. For a detailed description and parameters, please refer to the Supplementary Information.

Preparation of the GPAP and other SGPs. The whole fabrication process of the GPAP is so simple that it could be finished using regular kitchen apparatus. Ca(NO₃)₂·4H₂O (analytical purity) was obtained from Sinopharm Chemical Reagent, and waxy starch (amylopectin > 90%) was purchased from Qinhuangdao Lihua Starch. For preparation of the GPAP, we used a fixed water-to-starch mass ratio of 5 (for example, 1 g deionized water added with 0.2 g starch), and the crosslinker Ca(NO₃)₂·4H₂O was dissolved in the water at a mass concentration of 33.3%. The mixture was stirred at 60 °C to obtain a viscous gel. To remove the bubbles in the gel, the stirring process was completed in the vacuum container. The freshly prepared gel was stabilized at 37 °C and 50% relative humidity for 2 d, to evaporate excessive water and obtain a stable gel. The stabilization process can also be completed by leaving the gel in ambient conditions for various time periods, depending on the temperature and relative humidity. To obtain gel with specific geometries for various tests, the gel was cast into a container-like petri dish to form a film of the desired thickness, and the gel film could be cut into the desired geometry and sizes. The GPAP was characterized by Fourier-transform infrared spectroscopy and X-ray diffraction. Its water retention capability was also tested. For detailed methods, see the Supplementary Information.

For the preparation of SGPs with different mechanical properties but almost the same composition, we kept the fixed water-to-starch mass ratio of 5 but slightly altered the mass concentration of starch from 11.1% (GPAP) to 13.3% (SGP1) and 15.4% (SGP2), while the content of the crosslinker was adjusted accordingly. The rest of the preparation process was the same as for preparing the GPAP. Due to the existence of ionic crosslinker and water, the GPAP and SGPs were not insulators, but they had low conductivity (10^{-4}–10^{-3} S m^{-1})—much lower than that of myocardium (0.2–0.6 S m^{-1} according to refs. [60,61]).

Mechanical property of the GPAP. First, we performed tensile tests on the GPAP using a constant strain rate mode at 60 mm min^{-1} on a universal testing machine (HY10000; Shanghai Precision Instrument). The GPAP samples were moulded into a strip with an original length of 7 mm, a width of 30 mm and a thickness of 2 mm. The curves were fitted with the neo-Hookean model using data up to 500% strain.

For cyclic stretching tests, we first stretched the GPAP strips to a pre-stretch value of 50% (from an original length of 6.6–10 mm) or 100% (from an original length of 5–10 mm) at 300 mm min^{-1}. Then, we unloaded the strips to 8 mm and re-loaded them to 10 mm for 5,000 cycles at a speed of 75 cycles min^{-1}. To plot the stress–strain cycles, 8 mm was set as the original length of the strips (strain = 0) and 10 mm was the stretched length (maximum strain = 25%). To show the mechanical stability of the GPAP, a GPAP strip after cyclic stretching for 2,000 cycles (that is, when the GPAP reached the steady state) was retrieved and a tensile test was run as described above. Its stress–strain curve was then plotted (Fig. 2b). For detailed methods on rheological characterization and stress relaxation tests, see the Supplementary Information.

Characterization of adhesiveness and adhesion of the GPAP on porcine epicardium. We measured the adhesiveness of different gels on porcine epicardium using a universal testing machine with the method modified from the ASTM standard C907-17. Besides GPAP and SGPs, commercially available adhesive gels including fibrin glue (Guangzhou Bioseal Biotech), cyanoacrylate glue (Beijing Compont Medical Devices) and collagen (type I collagen from a bovine tendon; Shanghai YuanYe Biotechnology) were also tested. Collagen gel was prepared by dissolving collagen into water followed by drying in an oven until gel-like collagen formed. The conformability of the GPAP adhered to porcine epicardium was also tested (for detailed methods, see the Supplementary Information).

We flattened and fixed fresh porcine epicardia (each piece with an area of 1.6 cm^2) on both the upper and lower crossheads in a universal testing machine. First, we placed the gel (1 mm in thickness) to cover the epicardium fixed on the lower crosshead. We then lowered the upper crosshead until the upper epicardium fully connected with the gel and a small compression force of 0.1 N was reached. When the force was relaxed to 0, we started to separate the crossheads at a speed of 60 mm min^{-1}, and the stress–displacement curve was recorded. Interfacial strength was defined as the maximum stress during the separation process. Interfacial toughness was defined as the amount of energy required to detach a unit area of gel (1 mm thick) from the epicardium, which was calculated by integrating the stress–displacement curve. Three distinct samples were tested for all groups.

In vitro cytocompatibility tests. We evaluated the cytocompatibility of the GPAP, SGPs and cyanoacrylate glue by culturing cells in the extracts of the gels. Gels were sterilized by ^{60}Co irradiation of 20 kGy for 48 h and immersed in cell culture medium (Dulbecco's modified Eagle's medium with 10 vol.% foetal bovine serum and 1 vol.% penicillin-streptomycin solution) at concentrations of 10 and 20 mg ml^{-1} for 1 d. The concentrations were selected according to several previous studies on similar adhesive materials[62–65]. We then collected the extracts and filtrated them through a 0.22 μm membrane filter (Millex-GP; Millipore) to obtain a test medium before the cell tests. Regular cell culture medium (Dulbecco's modified Eagle's medium with 10 vol.% foetal bovine serum and 1 vol.% penicillin-streptomycin solution) was used for the control group (control medium). Cells were all purchased from the Stem Cell Bank of the Chinese Academy of Sciences.

We seeded H9C2 rat cardiomyocytes (density: 4,500 cells well^{-1}) or NIH/3T3 fibroblasts (density: 5,000 cells well^{-1}) in 96-well plates and filled each well with 200 μl of regular cell culture medium. Cells were cultured under a humidified atmosphere of 5% CO$_2$ at 37 °C. After 1 d, we replaced the cell culture medium with gel extracts and continued to culture the cells for 1 and 3 d. In the control group, we replaced the cell culture medium with the regular medium. After prescribed time periods, we removed the medium in each well and rinsed the well with phosphate buffered saline twice. We then added 10 μl of Cell Counting Kit-8 (Dojindo Molecular Technologies) solution together with 100 μl of phosphate buffered saline to each well. After incubating at 37 °C for 2 h, we transferred the 110 μl of solution to a new 96-well plate and measured the optical density (OD) of the solution at 450 nm on a micro-plate reader (PowerWave X; BioTek). The cell viability was calculated by:

$$\text{Cell viability} = \text{OD}_{\text{extract}}/\text{OD}_{\text{control}} \times 100\%$$

where $\text{OD}_{\text{extract}}$ is the OD value of the extract group and $\text{OD}_{\text{control}}$ is the OD value of the control group. The cell tests were repeated five times for cardiomyocytes and four times for fibroblasts, with three replicas for each time.

To visualize the cell viability, we cultured the cells with GPAP extract in the 24-well plate (seeding density: 10,000 cells cm^{-2}) as described above. After 1 and 3 d, the cells were stained with a LIVE/DEAD viability kit (Thermo Fisher Scientific) and observed by fluorescence microscopy (EVOS, AMG).

Animals. We used Sprague–Dawley rats (male, about 250 g in weight) that were obtained from the Laboratory Animal Care Facility of Shanghai Medical College, Fudan University. All procedures involving animal use, housing and operations were approved in the *Guide for the Care and Use of Laboratory Animals* 8th edn (National Institutes of Health, Nat. Acad. Press, 2011) and carried out under the supervision of the Fudan University Institutional Animal Care and Use Committee (approval number 20150119-013).

In vivo biocompatibility tests. We divided healthy Sprague–Dawley rats into three groups: healthy (no GPAP); healthy + GPAP; and healthy + cyanoacrylate gel. After anaesthesia and thoracotomy, the pericardium was removed in the healthy + GPAP and healthy + cyanoacrylate gel groups. In the healthy + GPAP group, we used tweezers to stretch the GPAP (Supplementary Video 1) to a width of about 1.1 cm, then patched the GPAP onto the epicardium. In the healthy + cyanoacrylate gel group, we covered the cyanoacrylate gel on the epicardium with a dropper.

Induction of MI in Sprague–Dawley rats and treatment with gel patches. The LAD coronary artery of Sprague–Dawley rats was occluded to induce MI injury. In brief, after anaesthesia and thoracotomy, the pericardium was removed and a 6-0 suture was placed under the LAD coronary artery. In the acute MI model study, animals were randomized into four groups: MI, MI + GPAP, MI + SGP1 and MI + SGP2. For the subacute MI models, animals were randomized into two groups: MI and MI + GPAP. In the MI group, animals were exposed to open-chest surgery with LAD coronary artery ligation but without GPAP treatment. In the MI + GPAP and MI + SGP1 groups, each time, we used a clump of gel with the same mass and size, stretched the clump to a width of about 1.1 cm with tweezers and then patched onto the MI site of the heart. In the MI + SGP2 group, because the adhesiveness of SGP2 was not sufficient to maintain a robust adhesion on the beating heart, SGP2 was first patched onto the MI site using a similar procedure, then the edge of SGP2 was glued using cyanoacrylate glues.

RNA-Seq experiment. We extracted total RNA of tissues from MI sites for both the MI and MI + GPAP groups using TRIzol (Invitrogen) from the acute rat MI models. In the sham group, tissues from the similar left ventricle site in the MI group were used. Poly-A containing mRNA was then purified using poly-T oligo-linked magnetic beads from the 1 μg total RNA. After purification, mRNAs were fragmented into small fragments using divalent cations at elevated temperatures. Fragmented mRNAs were synthesized on the first-strand complementary DNA (cDNA) using reverse transcriptase and random primers. The second-strand cDNA was then synthesized using DNA polymerases I and RNase H. These cDNA fragments were then subjected to an end repair process by adding a single 'A' base, followed by ligation of the adaptors. These products were then purified and enriched with PCR to create the final cDNA library. The RNA concentration of the library was then determined using the Qubit RNA Assay Kit in Qubit 3.0 for preliminarily quantification, and then diluted to 1 ng μl^{-1}. The insert size was assessed using the Agilent 2100 Bioanalyzer system (Agilent Technologies) and the qualified insert size was accurately quantified using a StepOnePlus Real-Time PCR System (library valid concentration > 10 nM). The clustering of the index-coded samples was performed on a cBot cluster generation system using a HiSeq PE Cluster Kit v4-cBot-HS (Illumina) according to the manufacturer's instructions. After cluster generation, the libraries were sequenced on an Illumina HiSeq 4000 platform, and 150-base pair paired-end reads were generated. The web-based OmicsBean microarray data analysis system was used for raw data variance modelling and statistical testing. The MI + GPAP group was compared with the MI group using unpaired Student's t-tests. OmicsBean was also used for gene ontology analyses, as well as principle component analyses.

Quantitative real-time PCR. We extracted the total RNA using the TRIzol reagent (Life Technologies) according to the manufacturer's instructions. RNA (2 ng) was reverse-transcribed into cDNA using the AMV Reverse Transcription System (Promega). Quantitative reverse transcription PCR was performed with the SYBR Green quantitative PCR system (Shanghai Bioscience Co. Ltd.) with glyceraldehyde 3-phosphate dehydrogenase as an internal control.

Echocardiography. We examined the left ventricle contractile performance by echocardiography on a Vevo 770 imaging system (VisualSonics) equipped with a 30 MHz transducer. Short-axis views were obtained, and both conventional two-dimensional images and M-Mode images were captured at the level of midpapillary muscle, as described previously. Measurements of the LVISD and LVIDD in M-mode were performed.

Electrocardiography. After anaesthesia, rat limbs were fixed on the operating table with rubber bands. Needle electrodes were inserted subcutaneously into the limbs. The parameters were set as follows: tracing speed 50 mm s^{-1}; voltage 2 mV; recording time 5 min.

Haemodynamic measurement. Left ventricle haemodynamics were evaluated using a PowerLab system (ADInstruments) with a micronanometric catheter advanced into the left ventricle of rats through the right common carotid artery and aorta. Left ventricular end-diastolic pressure (LVEDP) and end-systolic pressure (LVESP), maximal dP/dt and minimal dP/dt were then obtained according to the manufacturer's manual. ΔP here was taken as the difference between the LVESP and LVEDP.

Micro-computed tomography. Rats were sedated with 1.5–2.0% isoflurane in oxygen (60 ml min^{-1}). Radionuclide imaging was performed using a dual-headed μSPECT (PerkinElmer) gamma camera with micro-computed tomography.

Histology and immunofluorescence staining. Rat cadaveric hearts were fixed, paraffin-embedded and sectioned, followed by haematoxylin and eosin staining (G1005; Servicebio) and Masson's trichrome staining (G1006; Servicebio). Fixed hearts were embedded into optimal cutting temperature compound (O.C.T.; Sakura Finetek), frozen and sectioned into 8-μm-thick sections. The slides were permeabilized with 0.5% Triton X-100 for 15 min, and blocked with normal goat serum for 30 min. The slides were then incubated with appropriate primary antibodies at 4 °C overnight. Last, the samples were washed three times and stained with the appropriate secondary antibodies and 4′,6-diamidino-2-phenylindole (DAPI). Before imaging, all slides were covered with cover glass in hardening mounting medium. Antibody details can be found in the Reporting Summary. Cells and sections were counterstained with DAPI or Alexa Fluor 488 Conjugate Wheat Germ Agglutinin (Thermo Fisher Scientific) per the manufacturer's protocol. Tissue images were recorded with a fluorescence microscope (DMi8; Leica).

Measurements of infarction size and wall thickness. The infarction size was determined as the average of 5 sections at 2 mm intervals sampled from the apex from the formula infarct size: (coronal infarct perimeter (epicardial + endocardial)/ total coronal perimeter (epicardial + endocardial)) × 100.

The left ventricular wall thickness was determined as the average thickness of the left ventricle wall of 5 sections at 2 mm intervals sampled from the apex, each measured from 30 cross-sections along the left ventricle wall.

Statistical analysis. Means and standard deviations of the data are presented. To compare the differences between two groups, two-tailed unpaired Student's t-tests calculated with Prism software were used. Differences were considered significant at $P < 0.05$.

Reporting Summary. Further information on research design is available in the Nature Research Reporting Summary linked to this article.

Data availability
All data supporting the findings of this study are available within the paper and its Supplementary Information files. Source data for the figures are available from the corresponding authors upon reasonable request. The RNA sequence data have been deposited in the National Center for Biotechnology Information Sequence Read Archive, with accession code SRP187341.

Code availability
The FEBio code is available upon reasonable request.

References
1. Rane, A. A. & Christman, K. L. Biomaterials for the treatment of myocardial infarction: a 5-year update. *J. Am. Coll. Cardiol.* **58**, 2615–2629 (2011).
2. Laflamme, M. A. & Murry, C. E. Heart regeneration. *Nature* **473**, 326–335 (2011).
3. Wei, K. et al. Epicardial FSTL1 reconstitution regenerates the adult mammalian heart. *Nature* **525**, 479–485 (2015).
4. Shadrin, I. Y. et al. Cardiopatch platform enables maturation and scale-up of human pluripotent stem cell-derived engineered heart tissues. *Nat. Commun.* **8**, 1825 (2017).
5. Fujimoto, K. L. et al. An elastic, biodegradable cardiac patch induces contractile smooth muscle and improves cardiac remodeling and function in subacute myocardial infarction. *J. Am. Coll. Cardiol.* **49**, 2292–2300 (2007).
6. Didie, M. et al. Parthenogenetic stem cells for tissue-engineered heart repair. *J. Clin. Invest.* **123**, 1285–1298 (2013).
7. Liao, S.-Y. et al. Attenuation of left ventricular adverse remodeling with epicardial patching after myocardial infarction. *J. Card. Fail.* **16**, 590–598 (2010).
8. Stuckey, D. J. et al. Magnetic resonance imaging evaluation of remodeling by cardiac elastomeric tissue scaffold biomaterials in a rat model of myocardial infarction. *Tissue Eng. Part A* **16**, 3395–3402 (2010).
9. Fujimoto, K. L. et al. Placement of an elastic biodegradable cardiac patch on a subacute infarcted heart leads to cellularization with early developmental cardiomyocyte characteristics. *J. Card. Fail.* **18**, 585–595 (2012).
10. Chi, N.-H., Yang, M.-C., Chung, T.-W., Chou, N.-K. & Wang, S.-S. Cardiac repair using chitosan-hyaluronan/silk fibroin patches in a rat heart model with myocardial infarction. *Carbohydr. Polym.* **92**, 591–597 (2013).
11. Serpooshan, V. et al. The effect of bioengineered acellular collagen patch on cardiac remodeling and ventricular function post myocardial infarction. *Biomaterials* **34**, 9048–9055 (2013).
12. Vilaeti, A. D. et al. Short-term ventricular restraint attenuates post-infarction remodeling in rats. *Int. J. Cardiol.* **165**, 278–284 (2013).
13. D'Amore, A. et al. Bi-layered polyurethane—extracellular matrix cardiac patch improves ischemic ventricular wall remodeling in a rat model. *Biomaterials* **107**, 1–14 (2016).
14. Moainie, S. L. et al. Infarct restraint attenuates remodeling and reduces chronic ischemic mitral regurgitation after postero-lateral infarction. *Ann. Thorac. Surg.* **74**, 444–449 (2002).
15. Fomovsky, G. M., Clark, S. A., Parker, K. M., Ailawadi, G. & Holmes, J. W. Anisotropic reinforcement of acute anteroapical infarcts improves pump function. *Circ. Heart Fail.* **5**, 515–522 (2012).
16. Enomoto, Y. et al. Early ventricular restraint after myocardial infarction: extent of the wrap determines the outcome of remodeling. *Ann. Thorac. Surg.* **79**, 881–887 (2005).
17. Clarke, S. A., Ghanta, R. K., Ailawadi, G. & Holmes, J. W. in *Cardiovascular and Cardiac Therapeutic Devices* (ed. Franz, T.) 169–206 (Springer Berlin Heidelberg, 2014).
18. Clarke, S. A., Goodman, N. C., Ailawadi, G. & Holmes, J. W. Effect of scar compaction on the therapeutic efficacy of anisotropic reinforcement following myocardial infarction in the dog. *J. Cardiovasc. Transl. Res.* **8**, 353–361 (2015).
19. Piao, H. et al. Effects of cardiac patches engineered with bone marrow-derived mononuclear cells and PGCL scaffolds in a rat myocardial infarction model. *Biomaterials* **28**, 641–649 (2007).
20. Sarig, U. et al. Natural myocardial ECM patch drives cardiac progenitor based restoration even after scarring. *Acta Biomater.* **44**, 209–220 (2016).
21. Gu, X. et al. Sustained viral gene delivery from a micro-fibrous, elastomeric cardiac patch to the ischemic rat heart. *Biomaterials* **133**, 132–143 (2017).
22. Mazza, E. & Ehret, A. E. Mechanical biocompatibility of highly deformable biomedical materials. *J. Mech. Behav. Biomed. Mater.* **48**, 100–124 (2015).
23. Winter, H. H. & Chambon, F. Analysis of linear viscoelasticity of a crosslinking polymer at the gel point. *J. Rheol.* **30**, 367–382 (1986).
24. Chambon, F. & Winter, H. H. Linear viscoelasticity at the gel point of a crosslinking PDMS with imbalanced stoichiometry. *J. Rheol.* **31**, 683–697 (1987).
25. Zhang, Y. S. & Khademhosseini, A. Advances in engineering hydrogels. *Science* **356**, eaaf3627 (2017).
26. Yuk, H., Zhang, T., Lin, S., Parada, G. A. & Zhao, X. Tough bonding of hydrogels to diverse non-porous surfaces. *Nat. Mater.* **15**, 190–196 (2016).
27. Oz, M. C. et al. Global surgical experience with the acorn cardiac support device. *J. Thorac. Cardiov. Sur.* **126**, 983–991 (2003).
28. Ghanta, R. K. et al. Adjustable, physiological ventricular restraint improves left ventricular mechanics and reduces dilatation in an ovine model of chronic heart failure. *Circulation* **115**, 1201–1210 (2007).
29. Ende, N. Amylase activity in body fluids. *Cancer* **14**, 1109–1114 (1961).
30. Omens, J. H., Mackenna, D. A. & Mcculloch, A. D. Measurement of strain and analysis of stress in resting rat left-ventricular myocardium. *J. Biomech.* **26**, 665–676 (1993).
31. Lin, Y. D. et al. A nanopatterned cell-seeded cardiac patch prevents electro-uncoupling and improves the therapeutic efficacy of cardiac repair. *Biomater. Sci.* **2**, 567–580 (2014).
32. Kutschka, I. et al. Collagen matrices enhance survival of transplanted cardiomyoblasts and contribute to functional improvement of ischemic rat hearts. *Circulation* **114**, I167–I173 (2006).
33. Simpson, D., Liu, H., Fan, T. H., Nerem, R. & Dudley, S. C. Jr. A tissue engineering approach to progenitor cell delivery results in significant cell engraftment and improved myocardial remodeling. *Stem Cells* **25**, 2350–2357 (2007).
34. Liang, S. et al. Paintable and rapidly bondable conductive hydrogels as therapeutic cardiac patches. *Adv. Mater.* **30**, e1704235 (2018).
35. Efraim, Y. et al. Biohybrid cardiac ECM-based hydrogels improve long term cardiac function post myocardial infarction. *Acta Biomater.* **50**, 220–233 (2017).
36. Ravi, S. et al. Effect of bone marrow-derived extracellular matrix on cardiac function after ischemic injury. *Biomaterials* **33**, 7736–7745 (2012).
37. Jin, J. et al. Transplantation of mesenchymal stem cells within a poly(lactide-co-ε-caprolactone) scaffold improves cardiac function in a rat myocardial infarction model. *Eur. J. Heart Fail.* **11**, 147–153 (2009).

38. Giraud, M.-N. et al. Hydrogel-based engineered skeletal muscle grafts normalize heart function early after myocardial infarction. *Artif. Organs* **32**, 692–700 (2008).

39. Siepe, M. et al. Myoblast-seeded biodegradable scaffolds to prevent post-myocardial infarction evolution toward heart failure. *J. Thorac. Cardiovasc. Sur.* **132**, 124–131 (2006).

40. Hashizume, R. et al. The effect of polymer degradation time on functional outcomes of temporary elastic patch support in ischemic cardiomyopathy. *Biomaterials* **34**, 7353–7363 (2013).

41. Mewhort, H. E. M. et al. Bioactive extracellular matrix scaffold promotes adaptive cardiac remodeling and repair. *JACC Basic Transl. Sci.* **2**, 450–464 (2017).

42. Singelyn, J. M. et al. Catheter-deliverable hydrogel derived from decellularized ventricular extracellular matrix increases endogenous cardiomyocytes and preserves cardiac function post-myocardial infarction. *J. Am. Coll. Cardiol.* **59**, 751–763 (2012).

43. Dai, W. et al. Intramyocardial injection of heart tissue-derived extracellular matrix improves postinfarction cardiac function in rats. *J. Cardiovasc. Pharmacol. Ther.* **18**, 270–279 (2013).

44. Hassaballah, A. I., Hassan, M. A., Mardi, A. N. & Hamdi, M. An inverse finite element method for determining the tissue compressibility of human left ventricular wall during the cardiac cycle. *PLoS ONE* **8**, e82703 (2013).

45. Wang, H. M. et al. Structure-based finite strain modelling of the human left ventricle in diastole. *Int. J. Numer. Meth. Bio.* **29**, 83–103 (2013).

46. Eriksson, T. S. E., Prassl, A. J., Plank, G. & Holzapfel, G. A. Influence of myocardial fiber/sheet orientations on left ventricular mechanical contraction. *Math. Mech. Solids* **18**, 592–606 (2013).

47. Gao, H., Carrick, D., Berry, C., Griffith, B. E. & Luo, X. Y. Dynamic finite-strain modelling of the human left ventricle in health and disease using an immersed boundary-finite element method. *IMA J. Appl. Math.* **79**, 978–1010 (2014).

48. Hall, J. E. *Guyton and Hall Textbook of Medical Physiology* (Elsevier Health Sciences, 2015).

49. Mielniczuk, L. M. et al. Left ventricular end-diastolic pressure and risk of subsequent heart failure in patients following an acute myocardial infarction. *Congest. Heart Fail.* **13**, 209–214 (2007).

50. Holzapfel, G. A. & Ogden, R. W. Constitutive modelling of passive myocardium: a structurally based framework for material characterization. *Phil. Trans. R. Soc. A* **367**, 3445–3475 (2009).

51. Guccione, J. M. & Mcculloch, A. D. Mechanics of active contraction in cardiac-muscle. 1. Constitutive relations for fiber stress that describe deactivation. *J. Biomech. Eng. Trans. ASME* **115**, 72–81 (1993).

52. Guccione, J. M., Waldman, L. K. & Mcculloch, A. D. Mechanics of active contraction in cardiac-muscle. 2. Cylindrical models of the systolic left-ventricle. *J. Biomech. Eng. Trans. ASME* **115**, 82–90 (1993).

53. Rodriguez, E. K., Omens, J. H., Waldman, L. K. & Mcculloch, A. D. Effect of residual stress on transmural sarcomere length distributions in rat left ventricle. *Am. J. Physiol.* **264**, H1048–H1056 (1993).

54. Walker, J. C. et al. Magnetic resonance imaging-based finite element stress analysis after linear repair of left ventricular aneurysm. *J. Thorac. Cardiov. Sur.* **135**, 1094–1102 (2008).

55. Goktepe, S., Abilez, O. J. & Kuhl, E. A generic approach towards finite growth with examples of athlete's heart, cardiac dilation, and cardiac wall thickening. *J. Mech. Phys. Solids* **58**, 1661–1680 (2010).

56. Himpel, G., Kuhl, E., Menzel, A. & Steinmann, P. Computational modelling of isotropic multiplicative growth. *CMES Comp. Model. Eng. Sci.* **8**, 119–134 (2005).

57. Genet, M., Lee, L. C., Baillargeon, B., Guccione, J. M. & Kuhl, E. Modeling pathologies of diastolic and systolic heart failure. *Ann. Biomed. Eng.* **44**, 112–127 (2016).

58. Puso, M. A. & Weiss, J. A. Finite element implementation of anisotropic quasi-linear viscoelasticity using a discrete spectrum approximation. *J. Biomech. Eng. Trans. ASME* **120**, 62–70 (1998).

59. Maas, S. A., Ellis, B. J., Ateshian, G. A. & Weiss, J. A. FEBio: finite elements for biomechanics. *J. Biomech. Eng. Trans. ASME* **134**, 011005 (2012).

60. Tsai, J. Z. et al. In-vivo measurement of swine myocardial resistivity. *IEEE Trans. Biomed. Eng.* **49**, 472–483 (2002).

61. Gabriel, C., Peyman, A. & Grant, E. H. Electrical conductivity of tissue at frequencies below 1 MHz. *Phys. Med. Biol.* **54**, 4863–4878 (2009).

62. Li, J. et al. Tough adhesives for diverse wet surfaces. *Science* **357**, 378–381 (2017).

63. Mehdizadeh, M., Weng, H., Gyawali, D., Tang, L. P. & Yang, J. Injectable citrate-based mussel-inspired tissue bioadhesives with high wet strength for sutureless wound closure. *Biomaterials* **33**, 7972–7983 (2012).

64. Guo, J. S. et al. Click chemistry improved wet adhesion strength of mussel-inspired citrate-based antimicrobial bioadhesives. *Biomaterials* **112**, 275–286 (2017).

65. Jeon, E. Y. et al. Rapidly light-activated surgical protein glue inspired by mussel adhesion and insect structural crosslinking. *Biomaterials* **67**, 11–19 (2015).

Acknowledgements

Author contributions

L.Y., N.S. and H.G. conceived and designed the study, analysed the data and provided funding. X.L., Y.B. and H.Y. carried out preparation and characterization of the GPAP, in vitro evaluation and data analysis. Y.L. performed the simulation work. A.B., H.C., W.J. and X.W. carried out the GPAP experiments for MI in rats, transcriptomic study and data collection. All authors wrote the manuscript.

Competing interests

The authors declare no competing interests.

Additional information

Supplementary information is available for this paper at https://doi.org/10.1038/s41551-019-0380-9.

Reprints and permissions information is available at www.nature.com/reprints.

Correspondence and requests for materials should be addressed to L.Y., N.S or H.G.

Publisher's note: Springer Nature remains neutral with regard to jurisdictional claims in published maps and institutional affiliations.

nature research

Corresponding author(s):   Huajian Gao, Lei Yang, Ning Sun

Last updated by author(s):   Jan 2, 2019

Reporting Summary

Nature Research wishes to improve the reproducibility of the work that we publish. This form provides structure for consistency and transparency in reporting. For further information on Nature Research policies, see Authors & Referees and the Editorial Policy Checklist.

Statistics

For all statistical analyses, confirm that the following items are present in the figure legend, table legend, main text, or Methods section.

n/a	Confirmed	
☐	☒	The exact sample size (*n*) for each experimental group/condition, given as a discrete number and unit of measurement
☐	☒	A statement on whether measurements were taken from distinct samples or whether the same sample was measured repeatedly
☐	☒	The statistical test(s) used AND whether they are one- or two-sided *Only common tests should be described solely by name; describe more complex techniques in the Methods section.*
☒	☐	A description of all covariates tested
☐	☒	A description of any assumptions or corrections, such as tests of normality and adjustment for multiple comparisons
☐	☒	A full description of the statistical parameters including central tendency (e.g. means) or other basic estimates (e.g. regression coefficient) AND variation (e.g. standard deviation) or associated estimates of uncertainty (e.g. confidence intervals)
☐	☒	For null hypothesis testing, the test statistic (e.g. *F*, *t*, *r*) with confidence intervals, effect sizes, degrees of freedom and *P* value noted *Give P values as exact values whenever suitable.*
☒	☐	For Bayesian analysis, information on the choice of priors and Markov chain Monte Carlo settings
☒	☐	For hierarchical and complex designs, identification of the appropriate level for tests and full reporting of outcomes
☒	☐	Estimates of effect sizes (e.g. Cohen's *d*, Pearson's *r*), indicating how they were calculated

Our web collection on statistics for biologists contains articles on many of the points above.

Software and code

Policy information about availability of computer code

Data collection	Open-sourced finite-element package FEBio and post-processing package Post-View were used for the finite-element modeling and data-collecting and processing, both of which are available online (https://febio.org)
Data analysis	Microsoft Excel, OriginPro 9, GraphPad QuickCalcs, Graphpad Prism, OmicsBean, Image J, and R and RStudio software programs were used.

For manuscripts utilizing custom algorithms or software that are central to the research but not yet described in published literature, software must be made available to editors/reviewers. We strongly encourage code deposition in a community repository (e.g. GitHub). See the Nature Research guidelines for submitting code & software for further information.

Data

Policy information about availability of data

All manuscripts must include a data availability statement. This statement should provide the following information, where applicable:

- Accession codes, unique identifiers, or web links for publicly available datasets
- A list of figures that have associated raw data
- A description of any restrictions on data availability

All data supporting the findings of this study are available within the papers and its Supplementary Information. Source data for the figures are available from the corresponding authors upon reasonable request. The RNA sequence data have been deposited in the National Center for Biotechnology Information Sequence Read Archive (SRA), with accession code SRP187341.

Field-specific reporting

Please select the one below that is the best fit for your research. If you are not sure, read the appropriate sections before making your selection.

☒ Life sciences ☐ Behavioural & social sciences ☐ Ecological, evolutionary & environmental sciences

For a reference copy of the document with all sections, see nature.com/documents/nr-reporting-summary-flat.pdf

Life sciences study design

All studies must disclose on these points even when the disclosure is negative.

Sample size	For the in vivo biocompatibility study, healthy Sprague-Dawley rats were divided into three groups (n=5 for Healthy without patching GPAP group, n=6 for Healthy+GPAP group and n=7 for Healthy+cyanoacrylate gel group).For the myocardial-infarction treatment study, Sprague-Dawley rats with LAD ligation were divided into four groups in the acute myocardial-infarction model and into two groups in the subacute myocardial-infarction model. These data were used to inform sample size (n=13 for MI and MI+GPAP group; n=5 for MI+SGP1 and MI+SGP2 each in acute myocardial infarction; n=6 for subacute myocardial infarction) for a sufficiently powered study to detect significant differences between treatment and control groups. For the transcriptomic study, Sprague-Dawley rats with LAD ligation were divided into two groups in the acute myocardial-infarction model (n=3 for MI and MI+GPAP group).
Data exclusions	There is no data exclusion for cell tests. The following exclusion criteria were pre-established: animals that did not survive the MI surgery, animals that did not display blanching of the left ventricle on LAD ligation and animals that had an ejection fraction greater than 60% as assessed by echocardiography after ligation. Male rats below 220 g or above 250 g and female rats were excluded.
Replication	At least 3 replications were performed for all the tests, and the attempts for replications were successful.
Randomization	All Sprague-Dawley rats were randomly divided into appropriate groups.
Blinding	Echocardiography imaging, electrocardiogram and haemodynamics measurements were conducted by an independent operator. The operator was blinded to group allocation during data collection and/or analysis.

Reporting for specific materials, systems and methods

We require information from authors about some types of materials, experimental systems and methods used in many studies. Here, indicate whether each material, system or method listed is relevant to your study. If you are not sure if a list item applies to your research, read the appropriate section before selecting a response.

Materials & experimental systems

n/a	Involved in the study
☐	☒ Antibodies
☐	☒ Eukaryotic cell lines
☒	☐ Palaeontology
☐	☒ Animals and other organisms
☒	☐ Human research participants
☒	☐ Clinical data

Methods

n/a	Involved in the study
☒	☐ ChIP-seq
☒	☐ Flow cytometry
☒	☐ MRI-based neuroimaging

Antibodies

Antibodies used

Heart sections were stained using the following antibodies:

Clone	Company	Lot number	Dilution	Species
CD3 monoclonal	Abcam	ab16669	1:100	rabbit
CD68 monoclonal	Abcam	ab31630	1:100	mouse
α-SMA polyclonal	Proteintech	55135-1-AP	1:100	rabbit
vWF polyclonal	Proteintech	11778-1-AP	1:100	rabbit
caspase-3 monoclonal	Abcam	ab32042	1:100	rabbit
α-actinin monoclonal	Abcam	ab9465	1:100	mouse
α-actinin polyclonal	Abcam	ab137346	1:100	rabbit
TNNT2 polyclonal	Proteintech	15513-1-AP	1:100	rabbit
Alexa Fluor 488 anti-mouse IgG	Proteintech	SA00013-1	1:200	goat
Alexa Fluor 488 anti-rabbit IgG	Proteintech	SA00013-2	1:200	goat
Alexa Fluor 594 anti-mouse IgG	Proteintech	SA00013-3	1:200	goat
Alexa Fluor 594 anti-rabbit IgG	Proteintech	SA00013-4	1:200	goat

Annexin V staining was conducted using the Annexin V-EGFP Apoptosis Detection Kit (Beyotime). Cells and sections were

counterstained with DAPI or AlexaFluor 488 Conjugate Wheat Germ Agglutinin (Thermo Fisher Scientific), per the manufacturer's protocol.

Validation

https://www.abcam.cn/cd3-antibody-sp7-ab16669.html
https://www.abcam.cn/cd68-antibody-ed1-ab31630.html
http://www.ptgcn.com/products/ACTA2-Smooth-muscle-Actin-Antibody-55135-1-AP.htm
http://www.ptgcn.com/Products/VWF-Antibody-11778-1-AP.htm
https://www.abcam.cn/active-caspase-3-antibody-e83-77-ab32042.html
https://www.abcam.cn/sarcomeric-alpha-actinin-antibody-ea-53-ab9465.html
https://www.abcam.cn/sarcomeric-alpha-actinin-antibody-ab137346.html
http://www.ptgcn.com/Products/TNNT2-Antibody-15513-1-AP.htm
http://www.ptgcn.com/products/CoraLite488—-conjugated-Affinipure-Goat-Anti-Mouse-IgG-H-L--secondary-antibody.htm
http://www.ptgcn.com/products/CoraLite488—-conjugated-Affinipure-Goat-Anti-Rabbit-IgG-H-L--secondary-antibody.htm
http://www.ptgcn.com/products/CoraLite594—-conjugated-Goat-Anti-Mouse-IgG-H-L--secondary-antibody.htm
http://www.ptgcn.com/products/CoraLite594—-conjugated-Goat-Anti-Rabbit-IgG-H-L--secondary-antibody.htm
http://www.beyotime.com/product/C1067S.htm

Eukaryotic cell lines

Policy information about cell lines

Cell line source(s)

NIH/3T3 fibroblasts (ATCC CRL-1658) and H9C2 rat cardiomyocytes (ATCC CRL-1446) were used. Cells were purchased from Stem Cell Bank, Chinese Academy of Sciences.

Authentication

Authentication of the NIH/3T3 cells and H9C2 cells was provided by the Stem Cell Bank, Chinese Academy of Sciences.

Mycoplasma contamination

Cells were tested, and absence of mycoplasma contamination was confirmed.

Commonly misidentified lines
(See ICLAC register)

No commonly misidentified cell lines were used.

Animals and other organisms

Policy information about studies involving animals; ARRIVE guidelines recommended for reporting animal research

Laboratory animals

Sprague-Dawley rats (6–8 weeks old, male, about 220–250g of weight, Laboratory Animal Care Facility of Shanghai Medical College, Fudan University)

Wild animals

The study did not involve wild animals.

Field-collected samples

Porcine cadaver hearts were purchased from a local grocery market.

Ethics oversight

All procedures involving animal use, housing, and operations were approved by the Guide for the Care and Use of Laboratory Animals (National Institutes of Health, Publication No. 85-23, Revised), and carried out under the supervision of the Fudan University Institutional Animal Care and Use Committee (Approval No. 20150119-013).

Note that full information on the approval of the study protocol must also be provided in the manuscript.